A polyaniline functionalized NiFeP nanosheet array-based electrochemical immunosensor using Au/Cu$_2$O nanocubes as a signal amplifier for the detection of SARS-CoV-2 nucleocapsid protein†

Liwei Bai,[a] Yufen Shi,[a] Xue Zhang,[a] Xiaowei Cao, [c] Jianhua Jia,[d] Huanhuan Shi*[b] and Wenbo Lu *[a]

Coronavirus disease 2019 (COVID-19) is an infectious disease caused by severe acute respiratory syndrome coronavirus 2 (SARS-CoV-2), which emerged as a novel pathogen in 2019. The virus is responsible for a severe acute respiratory syndrome outbreak, affecting the respiratory system of infected individuals. COVID-19 is a super amplifier of basic diseases, and the disease with basic diseases is often more serious. Controlling the spread of the COVID-19 pandemic relies heavily on the timely and accurate detection of the virus. To resolve the problem, a polyaniline functionalized NiFeP nanosheet array-based electrochemical immunosensor using Au/Cu$_2$O nanocubes as a signal amplifier is fabricated for the detection of SARS-CoV-2 nucleocapsid protein (SARS-CoV-2 NP). Polyaniline (PANI) functionalized NiFeP nanosheet arrays are synthesized as an ideal sensing platform for the first time. PANI is coated on the surface of NiFeP by electropolymerization to enhance biocompatibility, beneficial for the efficient loading of the capture antibody (Ab$_1$). Significantly, Au/Cu$_2$O nanocubes possess excellent peroxidase-like activity and exhibit outstanding catalytic activity for the reduction of H$_2$O$_2$. Therefore, Au/Cu$_2$O nanocubes combine with a labeled antibody (Ab$_2$) through the Au–N bond to form labeled probes, which can effectively amplify current signals. Under optimal conditions, the immunosensor for the detection of SARS-CoV-2 NP shows a wide linear range of 10 fg mL^{-1}–20 ng mL^{-1} and a low detection limit of 1.12 fg mL^{-1} (S/N = 3). It also exhibits desirable selectivity, repeatability, and stability. Meanwhile, the excellent analytical performance in human serum samples confirms the practicality of the PANI functionalized NiFeP nanosheet array-based immunosensor. The electrochemical immunosensor based on the Au/Cu$_2$O nanocubes as a signal amplifier demonstrates great potential for application in the personalized point-of-care (POC) clinical diagnosis.

1. Introduction

Coronavirus disease 2019 (COVID-19) is a kind of infectious disease discovered in December 2019 and caused by the pathogen severe acute respiratory syndrome coronavirus 2 (SARS-CoV-2).[1,2] On 11th March 2020, the World Health Organization (WHO) declared the coronavirus disease a global pandemic.[3] The novel coronavirus with a long incubation period is highly contagious and has spread rapidly in more than 200 countries around the world.[4] It has seriously endangered human health and life safety, threatened global health systems, and affected the economic development of the international community. The main symptoms of COVID-19-infected patients are fever, cough, sore throat, shortness of breath, dyspnea and so on. Severe cases will even cause pneumonia, severe acute respiratory distress syndrome, renal failure, and death.[5,6] In addition, it should be noted that although asymptomatic infected patients do not show any signs of infection, there is still a huge risk of transmitting the virus to others. Hence, it is still of great significance to timely diagnose patients infected with SARS-CoV-2 and accurately

[a]Key Laboratory of Magnetic Molecules and Magnetic Information Materials (Ministry of Education), School of Chemistry and Material Science, Shanxi Normal University, Taiyuan 030031, China. E-mail: luwb@sxnu.edu.cn

[b]Institut für Quanten Materialien und Technologien, Karlsruher Institut für Technologie, Hermann-v.-Helmholtz-Platz 1, 76344 Eggenstein-Leopoldshafen, Germany. E-mail: huanhuan.shi@kit.edu

[c]Institute of Translational Medicine, Medical College, Yangzhou University, Yangzhou 225001, China

[d]College of Basic Medical Sciences, Chongqing Medical University, Chongqing 400016, China

screen carriers of the virus, for the purpose of effectively containing the global spread of the COVID-19 pandemic.

SARS-CoV-2 is a kind of enveloped, single-stranded RNA virus that is about 50–150 nm in diameter and 29 903 bp in length.[4] It contains four major structural proteins, namely the nucleocapsid (N) protein, spike (S) protein, membrane (M) protein, and envelope (E) protein.[3] Among them, N protein is the protein with high abundance and strong immunogenicity. Due to the characteristic of sequence conservation, it can serve as a biomarker to diagnose COVID-19.[6–9] Nowadays, the reverse transcription-polymerase chain reaction (RT-PCR) with high sensitivity and accuracy is considered as a gold standard to detect SARS-CoV-2 using the nasopharyngeal swab derived from patients.[10] Although the test results are accurate, a lengthy testing cycle, expensive equipment, professional laboratories, and trained professionals are required, which will greatly restrict the rapid detection of SARS-CoV-2.[11] Therefore, it is still extremely urgent to explore an accurate, rapid, and sensitive technique for the determination of SARS-CoV-2. Notably, the electrochemical immunoassay has been a kind of common detection technology for biomarkers in recent years, which depends on the specific recognition between antigens and antibodies.[12,13] Due to its high accuracy, high sensitivity, easy miniaturization, simple instrumentation, and low cost, it has attracted the widespread attention of many researchers.[7,14] Białobrzeska *et al.* constructed a new immunosensor for the detection of SARS-CoV-2 N protein based on the various surfaces of diamond/gold/glassy carbon. The obtained linear range was 4.4 ng ml^{-1}–4.4 pg mL^{-1}.[15] Yadav *et al.* successfully developed an electrochemical immunosensor based on the nanocomposites of polydopamine-modified molybdenum disulfide nanosheets to detect the SARS-CoV-2 N protein through electrochemical impedance spectroscopy.[16] However, although a lot of efforts have been made, exploiting effective signal amplification strategies with high sensitivity to detect SARS-CoV-2 N protein still remains a huge challenge.

It is well known that the performance of electrochemical immunosensors depends largely on the choice of modified electrode materials.[17,18] Recently, transition metal phosphides (TMPs), such as Ni_2P, Fe_2P and NiFeP, possess excellent electrical conductivity and metalloid characteristics, as well as rich active sites, showing excellent electrochemical performance.[19] Hence, TMPs have been widely used in the fields of electrolytic water,[20] supercapacitors,[21] and electrochemical sensors.[22] Many research studies have proved that bimetallic phosphides exhibit much higher electrocatalytic performance than single metal phosphides. However, over the past few years, the exploration of electrochemical immunosensors based on TMPs is very limited. To the best of our knowledge, no electrochemical immunosensor based on bimetallic NiFePs for the determination of SARS-CoV-2 N protein (SARS-CoV-2 NP) has been reported before. Furthermore, metal–organic frameworks (MOFs) are a class of new inorganic–organic hybrid materials composed of metal ions or metal clusters and multifunctional organic ligands.[23,24] They possess many advantages such as diverse composition, adjustable structures, high surface areas,

porosity, and abundant active sites.[25] Therefore, MOFs can serve as a kind of ideal precursor to prepare bimetallic TMPs. Whether the biorecognition molecules are immobilized effectively can also directly affect the performance of the immunosensor. Polyaniline (PANI), a typical conductive polymer, is deeply favored by researchers because of its unique proton doping, good stability, excellent conductivity, favorable biocompatibility, low cost, and simple synthesis.[26] Furthermore, it can be considered as a very promising candidate material for immunosensors, since plentiful amino groups of PANI are conducive to the effective fixation of biomolecules.[27] Therefore, it is a good strategy to combine bimetallic NiFeP with PANI to synthesize an efficient composite nanomaterial for the construction of a novel sandwich-type electrochemical immunosensor.

Inspired by the above discussion, the precursor of NiFe-MOF nanosheet arrays on Ni foam with a large surface area is synthesized by a simple hydrothermal reaction. It can be successfully transformed into bimetallic NiFeP nanosheet arrays using a low temperature phosphating reaction. Nanoarrays possess excellent conductivity and a large specific surface area, which can avoid the problem of blocking active sites caused by traditional adhesives.[28–30] Then, PANI is coated on the surface of NiFeP nanosheet arrays by a simple electrochemical polymerization method to obtain polyaniline functionalized NiFeP nanocomposites with good biocompatibility, for use as the substrate material for the sandwich-type electrochemical immunosensor to detect SARS-CoV-2 NP for the first time. In addition, Au nanoparticles decorated Cu_2O nanocubes (namely Au/Cu_2O) are synthesized as a signal amplification probe of the immunosensor. It is well known that Cu_2O possesses excellent peroxidase-like properties and can efficiently catalyze the reduction of H_2O_2.[31,32] The Au nanoparticles of Au/Cu_2O nanocubes can not only greatly improve the conductivity, but also enhance the biocompatibility facilitating the fixation of the secondary antibody (Ab$_2$) through Au–N bonding. The electrochemical signal generated by the reduction of H_2O_2 is recorded through *i–t* technology to achieve the quantitative detection of SARS-CoV-2 NP. Fig. 1 clearly illustrates the assembly process of a sandwich-type electrochemical immunosensor. Under optimal conditions, the immunosensor exhibits good performance with a wide linear range of 10 fg mL^{-1}–20 ng mL^{-1} and a detection limit of 1.12 fg mL^{-1} (S/N = 3). It can also realize the determination of SARS-CoV-2 NP in human actual serum samples, proving its broad application prospect in the aspect of clinical diagnosis and screening for novel coronavirus patients.

2. Experimental

2.1 Preparation of NiFe-MOF nanosheet arrays

The experimental reagents and apparatus used in this experiment are provided in the ESI.† NiFe-MOF nanosheet arrays (NiFe-MOFs/NF) are synthesized according to the method reported previously.[33] The nickel foam is ultrasonically treated
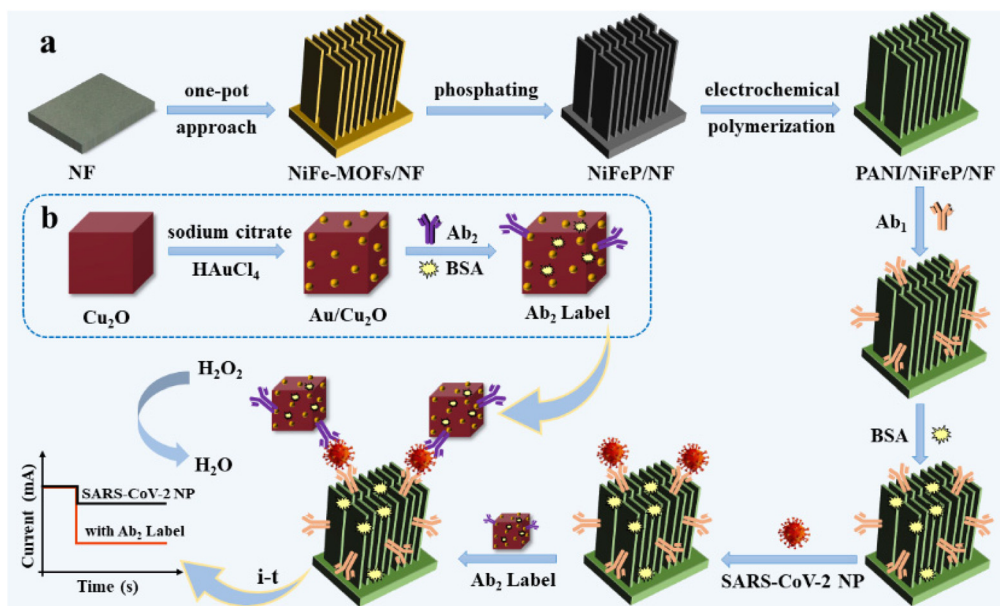
Fig. 1 (a) Schematic illustration of the fabrication process for the sandwich-type electrochemical immunosensor for the determination of SARS-CoV-2 NP. (b) The preparation process of the Ab_2-Au/Cu_2O signal probe.

in dilute HCl, acetone, ultrapure water, and ethanol separately for 10 min to remove the oxide layer on the surface. Concretely, 0.083 g of BDC was first dissolved in 5 mL of DMF ultrasonically and 15 mL of ethanol was added to form a uniform solution. Then, 0.082 g of $FeCl_3$ is dissolved in the above solution. The obtained yellow solution is transferred into a 25 mL Teflon-lined stainless-steel autoclave with a piece of treated nickel foam immersed vertically. The autoclave is sealed and kept at 140 °C for 12 h. Upon cooling to room temperature naturally, the obtained brown product is ultrasonically washed several times with ethanol and then dried under vacuum to obtain NiFe-MOF nanosheet arrays.

2.2 Preparation of NiFeP nanosheet arrays

The NiFe-MOFs/NF synthesized in the above step acted as a precursor, and it transformed into a NiFeP nanosheet array (NiFeP/NF) using a simple low-temperature phosphorization reaction. NaH_2PO_2 is placed upstream of the tube furnace, and NiFe-MOFs/NF is placed downstream of the furnace. It is heated for 2 h at 400 °C with a heating rate of 2 °C min^{-1}. Moreover, the whole procedure is carried out under an argon atmosphere. Finally, the brown precursors are successfully changed to black NiFeP nanosheet arrays.

2.3 Preparation of PANI functionalized NiFeP nanosheet arrays

An accessible electrochemical polymerization method is applied to prepare PANI functionalized NiFeP nanosheet arrays (PANI/NiFeP/NF). The NiFeP nanosheet arrays and Ag/AgCl (saturated KCl) are used as the working and reference electrodes, respectively. Pt wire served as the counter electrode. The polymerization process is performed by the cyclic voltam-

metry technique for 15 cycles in an electrolyte solution of 0.5 mol L^{-1} H_2SO_4 containing 0.2 mol L^{-1} aniline. Prior to polymerization, nitrogen is purged in the electrolyte for 5 min to remove oxygen. The voltage range is set as −0.3–1.0 V and the scan rate is 50 mV s^{-1}. Ultimately, the prepared PANI/NiFeP/NF is fully washed with ultrapure water.

2.4 Preparation of Au/Cu_2O nanocomposites

First, Cu_2O nanocubes are synthesized according to the previous method.[34] The whole experiment is carried out in a water bath at 55 °C. Firstly, 10 mL of NaOH aqueous solution (2.0 mol L^{-1}) is added dropwise to 100 mL of $CuCl_2 \cdot 2H_2O$ aqueous solution (0.01 mol L^{-1}). It can be observed that the solution gradually changes from clear light blue to cloudy bluish green until dark brown. After continuous stirring for 30 min, 10 mL of AA solution (0.6 mol L^{-1}) is added to the above solution. Then the solution is stirred for another 3 h. The precipitates are collected by centrifugation, washed with ultrapure water and ethanol, and dried in a vacuum to obtain Cu_2O nanocubes.

Then, Au/Cu_2O nanocomposites were prepared by a simple one-pot method.[35] At first, 98 mg of Cu_2O nanocubes synthesized previously and 260 mg of sodium citrate are completely dissolved in 65 ml of ultrapure water. 0.72 mL of 1% $HAuCl_4$ solution is added. The obtained brownish black precipitates are collected by centrifugation, and then dried in a vacuum at 60 °C.

2.5 Preparation of the Ab_2-Au/Cu_2O signal probe

The preparation process of the Ab_2-Au/Cu_2O signal probe is shown in Fig. 1b. Chiefly, 20 mg of the Au/Cu_2O nanocomposite was ultrasonically dissolved in 2.0 mL of PBS solu-

tion (pH = 7.4). 1.0 mL of Ab_2 (20.0 µg ml^{-1}) was added to the solution. Then the above solution was shaken continuously at room temperature for 12 h. The gold nanoparticles on Au/Cu_2O nanocomposites form a stable covalent bond with the –NH_2 of Ab_2 through the Au–N bond, enabling the efficient immobilization of Ab_2. Besides, 100 µL of 1% BSA solution was added to block non-specific binding sites, and shaken for another 3 h. Then the composites are centrifuged and re-dispersed in 2.0 mL of PBS solution (pH = 7.4). Eventually, the solution is stored at 4 °C for further use as a signal probe.

2.6 Fabrication of the sandwich-type immunosensor

Fig. 1 clearly demonstrates the step-by-step assembly process of the sandwich-type electrochemical immunosensor. At first, the PANI/NiFeP/NF with abundant amino groups served as the substrate material. 6.0 µL of 5% glutaraldehyde solution is modified on the electrode surface. Herein, glutaraldehyde can be used as a cross-linking agent to cross-link the amino groups between Ab_1 and the substrate material, showing that Ab_1 can be immobilized on the electrode surface. Then, 6.0 µL of 20.0 µg mL^{-1} Ab_1 is incubated at 37 °C for 40 min and the modified electrode is washed with PBS solution (pH = 7.4) to eliminate unbound Ab_1. Next, for the purpose of blocking the non-specific binding sites, 4.0 µL of 1% BSA was added onto the above electrode and fostered at 37 °C for 30 min, rinsing the electrode with PBS solution (pH = 7.4) to remove the redundant BSA. Subsequently, 6.0 µL of SARS-CoV-2 NP with different concentrations is incubated on the above modified electrode at 37 °C for 30 min *via* the specific binding between the antigen and the antibody. The electrode was washed with PBS solution (pH = 7.4) to remove the unbound antigen. Finally, 10.0 µL of the signal probe of Ab_2-Au/Cu_2O was added dropwise on the surface of the modified electrode and incubated at 37 °C for 50 min. The sandwich-type immunosensor was successfully assembled and stored at 4 °C for subsequent testing.

2.7 Detection of the SARS-CoV-2 nucleocapsid protein

All electrochemical experiments in this work were performed on a CHI660E electrochemical workstation (CH Instruments Ins., Chenhua, Shanghai). All measurements were performed in 0.1 mol L^{-1} PBS solution (Na_2HPO_4, NaH_2PO_4, pH = 6.50) with a common three-electrode system. The prepared modified electrode was used as the working electrode, the Ag/AgCl (saturated KCl) acted as the reference electrode, while the Pt sheet electrode served as the auxiliary electrode. The detection of SARS-CoV-2 NP by the assembled immunosensor is achieved by chronoamperometry (*i–t*) measurements with an applied voltage of −0.4 V. When the background current is kept steady, 5.0 mmol L^{-1} H_2O_2 which acted as an electroactive substance was added into the PBS solution under stirring. Then amperometry responses measured by *i–t* curves were recorded. It is noteworthy that the electrolyte solution was continuously stirred to facilitate mixing during the detection process.

3. Results and discussion

3.1 Characterization of PANI functionalized NiFeP nanosheet arrays

At first, bimetallic NiFe-MOF nanosheet arrays are synthesized by a simple solvothermal method, in which nickel foam served as the nickel source and substrate material, $FeCl_3$ acted as the iron source and BDC molecules acted as organic linkers. X-ray diffraction (XRD) is performed to study the crystal structure of the prepared NiFe-MOFs. Since the three diffraction peaks of Ni foam itself are too strong, the NiFe-MOF powder needs to be stripped from the substrate carefully. As shown in Fig. 2a, almost all the diffraction peaks of the obtained NiFe-MOF powder matched with the reported Ni-MOFs (CCDC: no. 638866).[33] Meanwhile, the diffraction peak located at $2\theta = 8.8°$ can well be indexed to the (200) crystal plane.[33,36,37] Compared with the reported Ni-MOFs, a partial shift of the diffraction peak of the bimetallic NiFe-MOFs may be caused by lattice distortion attributed to the doping of Fe atoms.

Scanning electron microscopy (SEM) was used to investigate the morphology of the synthesized bimetallic NiFe-MOFs. Fig. 2b–d show the SEM images at different magnifications. It can be clearly observed that nanosheet arrays grow on the surface of nickel foam uniformly. As illustrated in Fig. 2d, it is extremely interesting that each nanosheet unit is formed by two parallel nanosheets with an extremely obvious gap between them.

The chemical composition and valence state of bimetallic NiFe-MOF nanosheet arrays are further studied by X-ray photoelectron spectroscopy (XPS) analysis. Fig. 2e shows the XPS survey spectrum of NiFe-MOFs, which proves the existence of C, O, Ni, and Fe elements. In Fig. 2f, the XPS spectra of Fe 2p in NiFe-MOFs can be resolved into four peaks. There are two major peaks at 723.70 eV and 710.30 eV, which can be attributed to Fe $2p_{1/2}$ and Fe $2p_{3/2}$. It confirms that Fe species are in the +2 oxidation state in the obtained NiFe-MOFs.[38] The peaks located at 729.88 eV and 714.60 eV can be assigned to satellite peaks. As illustrated in Fig. 2g, the XPS spectra of Ni 2p reveal six characteristic peaks. The peaks located at 872.80 eV and 855.46 eV are respectively ascribed to Ni $2p_{1/2}$ and Ni $2p_{3/2}$, which correspond to Ni–O bonds connecting Ni ions and BDC molecules. The peaks at 874.15 eV (Ni $2p_{1/2}$) and 856.13 eV (Ni $2p_{3/2}$) are assigned to the Ni-OH bonds formed between Ni ions and hydroxyl groups. The other two peaks at 861.20 eV and 879.27 eV are attributed to the satellite peaks of Ni 2p.[33,39] In Fig. 2h, the XPS spectra of O 1s are fitted with two different peaks at 533.33 eV and 531.59 eV. The peak located at 533.33 eV is ascribed to the carboxylate groups (O–C=O) of the BDC organic linkers, while the other belongs to the Ni(Fe)–O bonds.[33]

As shown in Fig. 2i, functional groups contained in the synthesized NiNe-MOFs are investigated by Fourier transform infrared (FTIR) spectroscopy with a wavelength range of 2000–400 cm^{-1}. In Fig. 2i, the absorption peak located at 545 cm^{-1} corresponds to the Fe(Ni)–O bonds, which further confirms the successful coordination of the metal centers with
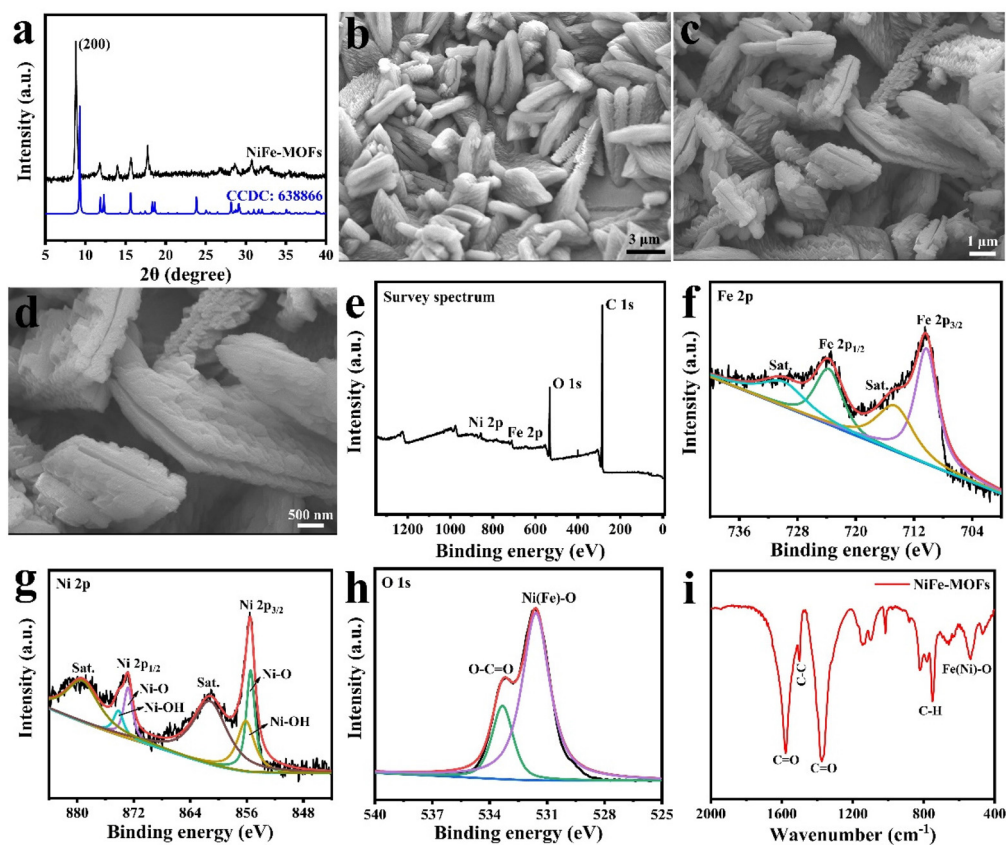
Fig. 2 (a) The XRD pattern of the NiFe-MOFs, stripped from the substrate carefully. (b–d) The SEM images of the NiFe-MOF nanosheet arrays at various magnifications. (e) The XPS survey spectrum of the prepared NiFe-MOFs. The XPS spectra of Fe 2p (f), Ni 2p (g), and O 1s (h). (i) The FTIR spectrum of the NiFe-MOFs.

the carboxylic groups (O–C=O) of BDC linkers. The absorption peak at 748 cm^{-1} indicates the vibration of the C–H bonds in the benzene ring. Meanwhile, the absorption peaks centered at 1579 cm^{-1} and 1373 cm^{-1} in the FTIR spectrum can be indexed to the asymmetric stretching vibration (ν_{as}) and symmetric stretching vibration (ν_s) of –COO–, respectively.[33,36] All of these results clearly verify that bimetallic NiFe-MOF nanosheet arrays are prepared successfully with the coordination between metal centers (Ni/Fe) and organic ligands (BDC).

The as-obtained bimetallic NiFe-MOF nanosheet arrays served as an ideal molecular platform for the design of high activity bimetallic NiFeP nanosheet arrays. It is achieved through a simple low-temperature phosphorylation reaction, while NaH$_2$PO$_2$ acts as a phosphorus source in this process. Fig. 3a displays the XRD pattern of the synthesized NiFeP nanosheet arrays. There are three strong diffraction peaks located at 44.58°, 51.94° and 76.46°, corresponding well to Ni foam (JCPDS: 04-0850).[40] Other obvious diffraction peaks are basically consistent with those of Fe$_2$P (JCPDS: 51-0943) and Ni$_2$P (JCPDS: 03-0953), while the main peaks are located between them, confirming the successful preparation of bimetallic NiFeP.[41,42]

SEM was carried out to study the surface morphology of the NiFeP derived from the NiFe-MOF precursor. As shown in

Fig. 3b and c, after the phosphorylation reaction, the NiFeP on Ni foam still maintains a uniform nanosheet morphology of the NiFe-MOF precursor. In Fig. 3d–f, the morphology of the nanosheet is further verified by transmission electron microscopy (TEM). Fig. 3g shows the elemental mapping image of the NiFeP nanosheet, which can be clearly seen that C, Fe, Ni, O and P elements are uniformly distributed throughout the whole nanosheet.

The chemical compositions of NiFeP nanosheet arrays are analyzed by energy dispersive spectroscopy (EDS) and XPS measurements. The EDS pattern shows the presence of Ni, Fe, P, C and O elements in Fig. S1.† Compared with the XPS survey spectrum of NiFe-MOFs, Fig. 4a shows the appearance of the P element which is consistent with the EDS result, further confirming that NiFe-MOFs are successfully converted into NiFeP. In Fig. 4b, the Ni 2p spectra can be resolved into six peaks. The two major peaks at 875.20 eV and 857.25 eV can be assigned to the Ni–O species and Ni–P species, respectively.[43] The peaks located at 880.54 eV and 862.22 eV belong to their relevant satellite peaks. Besides, two small peaks at 852.70 eV and 869.49 eV indicate metallic nickel.[43] The Fe 2p spectrum of NiFeP is shown in Fig. 4c. Two main peaks at 711.67 eV and 724.23 eV can be seen, which are assigned to Fe 2p$_{3/2}$ and Fe 2p$_{1/2}$, respectively. The peaks at 717.11 eV and
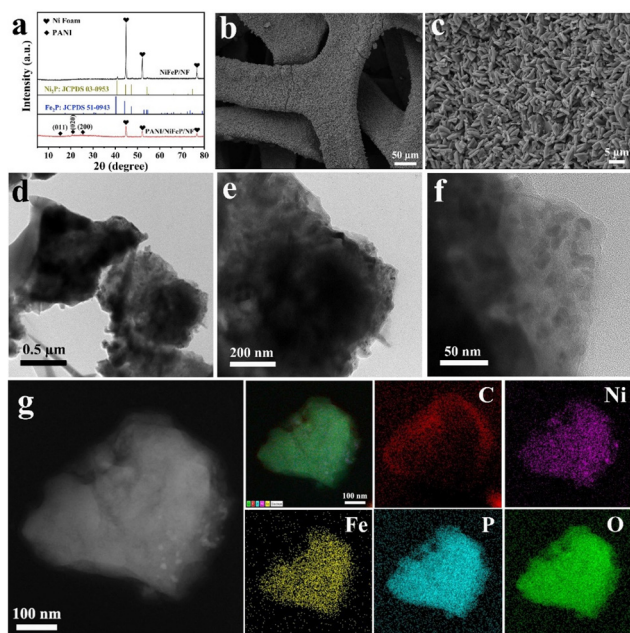
Fig. 3 (a) The XRD pattern of the NiFeP nanosheet arrays derived from NiFe-MOFs and the PANI/NiFeP nanosheet arrays. (b and c) The SEM patterns of the NiFeP nanosheet arrays with different magnifications. (d–f) The TEM images of the NiFeP nanosheet derived from NiFe-MOFs. (g) The EDX elemental mapping images of C, Ni, Fe, P and O for NiFeP nanosheets.
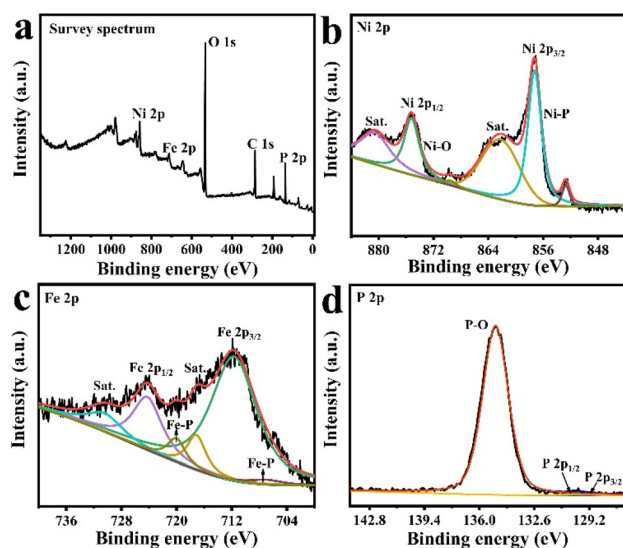

Fig. 4 (a) The XPS survey spectrum of the prepared NiFeP nanosheet arrays. The XPS spectra of Ni 2p (b), Fe 2p (c), and P 2p (d).

730.42 eV can be attributed to their shake-up satellite peaks and the peaks located at 707 eV and 720 eV are consistent with the Fe–P bonds of metal phosphides.[20] As displayed in Fig. 4d, the XPS spectra of P 2p can be fitted into three peaks, where the peak at 129.30 eV and 130.10 eV can be ascribed to the P $2p_{3/2}$ and P $2p_{1/2}$ of metal phosphides. The remaining peak

located at 129.30 eV corresponds to the P–O species of the oxidized phosphate formed on the surface of NiFeP, since the phosphide is extremely easily oxidized when exposed to air.[44] The above results demonstrate that NiFe-MOFs have been successfully converted into bimetallic NiFeP nanosheet arrays.

The aniline monomer is polymerized on the surface of NiFeP nanosheet arrays by electrochemical polymerization. Fig. 3a shows the XRD spectrum of PANI/NiFeP/NF. It can be found that there are three new characteristic diffraction peaks, corresponding to the (011), (020) and (200) crystal planes of PANI.[45] The surface morphology of PANI functionalized NiFeP is observed by SEM. As can be seen from Fig. S2a and S2b,† the surface of previous NiFeP nanosheet arrays has been covered with a thin film and a small number of nanoparticles, which preliminarily proves the successful modification of polyaniline. Fig. S2c† shows the cyclic voltammetry curves of aniline during polymerization on the surface of NiFeP. There are three pairs of redox characteristic peaks of polyaniline in CV curves. All the above results have proved the successful preparation of polyaniline functionalized NiFeP nanocomposites.

3.2 Characterization of Au/Cu₂O nanocomposites

The morphology of the synthesized Cu_2O and Au/Cu_2O nanocomposites was studied by SEM. Fig. 5a–c show the SEM images of the synthesized Cu_2O at different magnifications. It can be clearly seen that the synthesized Cu_2O exhibits a uniform nanocube morphology stacked by nanosheets. Fig. 5e and f reveal that the Au/Cu_2O nanocomposite still maintains the morphology of nanocubes, but the stacked nanosheets on the surface disappear, while Au nanoparticles are successfully loaded on the rough surface of the nanocubes. The microstructure of the Au/Cu_2O nanocomposite is further characterized by TEM. From Fig. 6a–c, it can be seen that the surface of Cu_2O nanocubes is uniformly loaded with Au nanoparticles. As shown in Fig. 6d, the high resolution transmission electron microscopy (HRTEM) image of the Au/Cu_2O nanocomposite exhibits clear lattice fringes with lattice spacings of 0.24 nm and 0.21 nm, corresponding to the (111) plane of Au and the (200) plane of Cu_2O, respectively.[35] From the elemental mapping images (Fig. 6e), it can be seen that Au, Cu and O elements are uniformly distributed on the surface of the Au/Cu_2O nanocomposite.

The crystal phases of Cu_2O and Au/Cu_2O are characterized using XRD measurement. As exhibited in Fig. 5d, the diffraction peaks at $2\theta = 29.53°$, $36.46°$, $42.41°$, $52.41°$, $61.32°$, $73.56°$ and $77.28°$ matched well with the (110), (111), (200), (211), (220), (331) and (222) planes of Cu_2O (JCPDS, no. 05-0667). There are no other impurity peaks found. Compared with Cu_2O, the XRD pattern of the Au/Cu_2O nanocomposite shows a diffraction peak located at 38.24° corresponding to the (111) crystal plane of Au (JCPDS, no. 04-0784).[35,46]

The XPS technology is used to study the surface chemical composition of Cu_2O and the Au/Cu_2O nanocomposite. In Fig. S3a† the XPS survey spectrum proves that the main elements on the surface of the Cu_2O nanocubes are Cu and
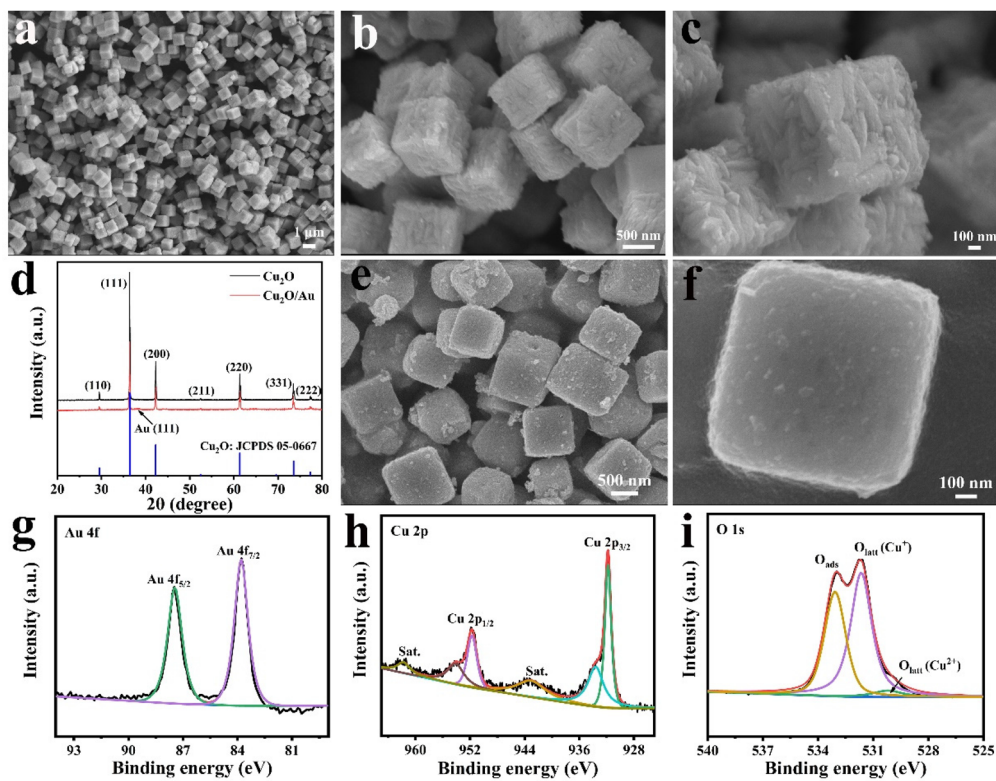
Fig. 5 (a–c) The SEM patterns of the Cu_2O nanocubes at different magnifications. (d) The XRD pattern of the obtained Cu_2O nanocubes and Au/ Cu_2O nanocomposite. (e and f) The SEM patterns of the Au/Cu_2O nanocomposite with different magnifications. The XPS spectra of Au 4f (g), Cu 2p (h), and O 1s (i) of the prepared Au/Cu_2O nanocomposite.
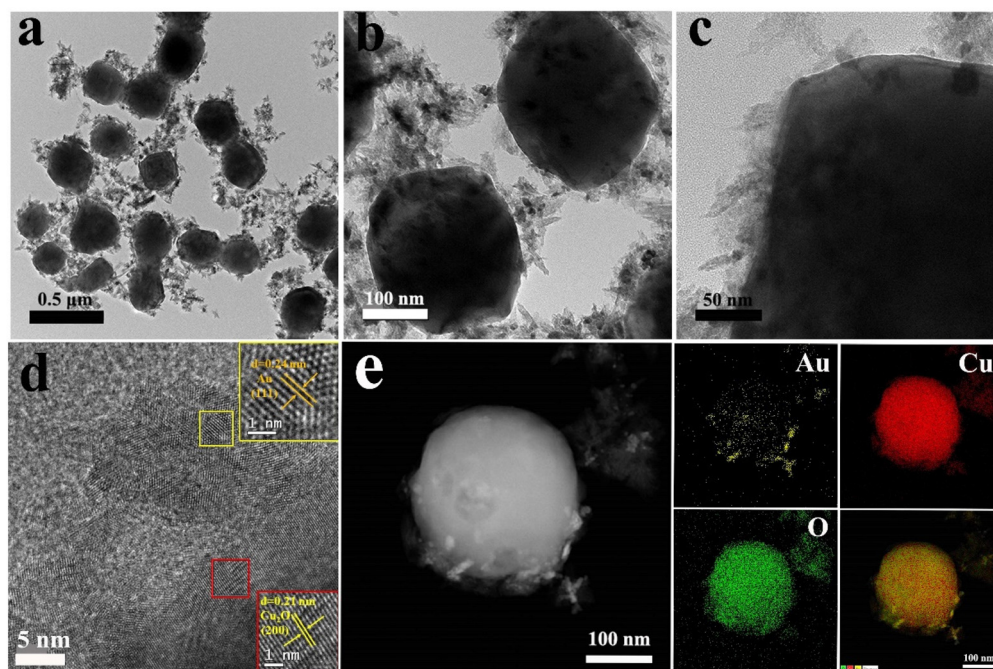

Fig. 6 (a–c) The TEM patterns of the obtained Au/Cu_2O nanocomposite at different magnifications. (d) The HRTEM image of the Au/Cu_2O nano-composite. (e) The EDX elemental mapping images of Au, Cu and O for the Au/Cu_2O nanocomposite.

O. As shown in Fig. S3b and S3c,† the XPS spectra of Cu 2p and O 1s further prove that the obtained Cu_2O was prepared successfully. Fig. S3d† shows that the main elements on the surface of the Au/Cu_2O nanocomposite are Cu, O and Au. The XPS spectrum of Au 4f in Fig. 5g displays two peaks at 87.45 eV and 83.80 eV, ascribed to Au $4f_{5/2}$ and Au $4f_{7/2}$, respectively. It proves that Au in Au/Cu_2O nanocomposite mainly exists in the state of metallic Au particles.[35,46] In Fig. 5h, the Cu 2p spectrum of Au/Cu_2O deconvolutes into six peaks. The peaks with binding energies of 931.80 eV and 951.72 eV can be assigned to Cu $2p_{3/2}$ and Cu $2p_{1/2}$, confirming that Cu exists mostly as Cu^+ in the obtained Au/Cu_2O nanocomposite. The peaks with lower intensities located at 933.60 eV and 954.10 eV correspond to Cu $2p_{3/2}$ and Cu $2p_{1/2}$, which indicates the presence of Cu^{2+} in the Au/Cu_2O nanocomposite. The existence of Cu^{2+} indicates that a small amount of Cu_2O is oxidized to convert into CuO.[47] The peaks located at 943.08 eV and 961.74 eV belong to their shake-up satellite peaks, respectively. As shown in Fig. 5i, the O 1s spectrum can be resolved into three peaks at 530.20 eV, 531.65 eV and 533.07 eV. The peak at 530.20 eV corresponds to the lattice oxygen of CuO, while the peak at 531.65 eV is attributed to the lattice oxygen of Cu_2O. The peak at 533.07 eV is ascribed to the surface adsorbed oxygen.[35,47] These results further confirm the successful preparation of Cu_2O nanocubes and the Au/Cu_2O nanocomposite.

3.3 Electrochemical characterization of the sandwich-type immunosensor

In order to investigate the layer-by-layer assembly process of the sandwich-type immunosensor for SARS-CoV-2 NP, the change of the current signal on the surface of the PANI/NiFeP/NF nanosheet array-electrode is recorded by chronoamperometry (i–t) measurement. Fig. 7a shows a series of i–t curves, and 5 mmol L^{-1} H_2O_2 was injected into PBS solution after the current remains stable. Then electrochemical signals obtained at different modified electrodes are recorded at −0.4 V. From Fig. 7a, the PANI/NiFeP/NF electrode (curve a) exhibits excellent electrocatalytic performance for the reduction of H_2O_2. After Ab_1 (curve b), BSA (curve c) and SARS-CoV-2 NP (curve d) are immobilized on the surface of the PANI/NiFeP/NF electrode

layer by layer, the current signal gradually decreased. This is because the poor conductivity of the protein film hinders the transfer of electrons. However, after Ab_2-Au/Cu_2O (curve e) is modified on the surface of the electrode, the current response signal is greatly enhanced. This is due to Au/Cu_2O possessing desirable electrochemical activity, which can greatly promote the reduction of H_2O_2 and effectively amplify the response current. In Fig. 7b, the corresponding bar chart can more clearly show the variation of the current response signal. The results prove that the proposed signal amplification strategy is both simple and effective, and the sandwich-type immunosensor for the detection of SARS-CoV-2 NP has been assembled successfully.

In addition, electrochemical impedance spectroscopy (EIS), a simple and effective measurement technique, can also be used to monitor the assembly process of immunosensors. The EIS measurement is carried out in 0.1 mol L^{-1} KCl solution containing 5 mmol L^{-1} $Fe(CN)_6^{3-/4-}$. As shown in Fig. S4,† PANI/NiFeP/NF (curve a) exhibits a small semicircle domain at high frequencies, indicating that polyaniline functionalized NiFeP nanosheet arrays possess excellent conductivity. When Ab_1 with poor conductivity is modified on the PANI/NiFeP/NF electrode surface, the diameter of the semicircle increased significantly (curve b), indicating that Ab_1 has been successfully immobilized on the electrode surface through a crosslinking agent. After BSA (curve c) and SARS-CoV-2 NP (curve d) are successively immobilized on the electrode surface, the semicircle diameter continues to increase gradually. This is because the above biomolecules hinder the transfer of electrons. Interestingly, after modifying the electrode surface with Ab_2-Au/Cu_2O (curve e), it can be observed that the diameter of the semicircle is significantly reduced. This is due to the excellent conductivity of Au nanoparticle modified Cu_2O nanocubes, which greatly promotes the transfer of electrons. The EIS results are consistent with i–t measurements, proving the successful assembly of the sandwich-type immunosensor and the feasibility of the proposed signal amplification strategy.

3.4 Optimization of the experimental conditions

In order to further improve the analytical performance of this immunosensor, the experimental conditions such as the pH of the PBS solution, the incubation temperature and incubation time of the antibody with the antigen and signal probe of Ab_2-Au/Cu_2O, the volume of the signal probe, and the concentration of injected H_2O_2 need to be optimized. In the optimized experiments, the immunosensor is prepared using the same concentration of SARS-CoV-2 NP (1.0 ng mL^{-1}). Under various conditions, corresponding i–t curves are recorded in order to monitor the change of electrochemical signals in time.

The pH value of PBS solution is one of the most important factors affecting the analytical performance of the immunosensor, which is mainly because the pH value can affect the affinity between protein molecules and electrode materials. Fig. S5† shows the change in the current signal of the immunosensor in a series of pH values of the PBS solution. As
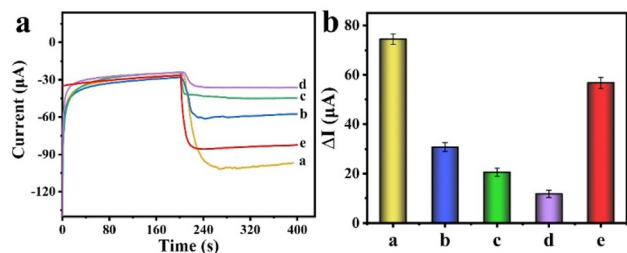

Fig. 7 (a) The i–t curves and (b) corresponding bar chart for the assembling steps of the sandwich-type immunosensor incubated with 1.0 ng mL^{-1} SARS-CoV-2 NP: (a) PANI/NiFeP/NF; (b) Ab_1/PANI/NiFeP/NF; (c) BSA/Ab_1/PANI/NiFeP/NF; (d) SARS-CoV-2 NP/BSA/Ab_1/PANI/NiFeP/NF; and (e) Ab_2-Au/Cu_2O/SARS-CoV-2 NP/BSA/Ab_1/PANI/NiFeP/NF.

shown in Fig. S5,† when the pH value of the PBS solution increases from 5.5 to 6.0, the current signal decreases, which may be due to polyaniline possessing better conductivity under acidic conditions. However, considering that the protein will deteriorate under strongly acidic or strongly alkaline conditions, the pH of 5.5 is not suitable for the construction of an immunosensor. When the pH value changes continuously from 6.0 to 8.0, the electrochemical signals increase first and then decrease, and current signal reaches the maximum at pH = 6.5. Therefore, an optimum pH of 6.5 is chosen in subsequent experiments.

Whether the antigen and antibody are effectively immobilized on the surface of electrode materials will also affect the performance of the immunosensor, which is related to the incubation time and incubation temperature. As revealed in Fig. 8a and c, when the incubation time gradually changes from 10 min to 60 min, the electrochemical signals both first increase and then gradually remain stable. When the incubation time is 30 min between Ab_1 and SARS-CoV-2 NP (Fig. 8a), the response current reaches the maximum. The maximum current signal is observed (Fig. 8c) when SARS-CoV-2 NP is incubated with Ab_2-Au/Cu_2O for 50 min. As displayed in Fig. 8b and d, when the incubation temperature varies from 4 °C to 50 °C, the electrochemical response currents increase initially and then decreased sharply. When the incubation temperature is 37 °C, the electrochemical signal reaches the maximum. This is because the specific binding of the immunosensor will be enhanced with the increase of temperature, however, excessive temperature will destroy the activity of protein biomolecules. Hence, the optimal incubation temperature of SARS-CoV-2 NP and Ab_2-Au/Cu_2O is selected as 37 °C in succeeding experiments. The optimal incubation times are chosen as 30 min and 50 min, respectively.

The content of the signal probe of Ab_2-Au/Cu_2O modified on the surface of the electrode material will also directly affect the sensitivity of the immunosensor. Therefore, it is extremely necessary to optimize the volume of the used Ab_2-Au/Cu_2O. As shown in Fig. 8e, when the volume of the used Ab_2-Au/Cu_2O increases from 0 μL to 12 μL, the electrochemical signals display the tendency to rise up at the beginning and decline later. When the volume of the signal probe is 10 μL, the electrochemical signal of the immunosensor reaches the maximum value. This confirms that 10 μL of Ab_2-Au/Cu_2O can maximize and catalyse the reduction of H_2O_2 and thus greatly amplify the corresponding electrochemical signals of the immunosensor for the determination of SARS-CoV-2 NP. Therefore, the optimal volume of the signal probe is selected as 10 μL in the subsequent construction process of the immunosensor.

In addition, the effect of the concentration of injected H_2O_2 on the performance of the immunosensor has also been investigated. As shown in Fig. 8f, when the concentration of injected H_2O_2 gradually increases from 2 mmol L^{-1} to 6 mmol L^{-1}, the electrochemical response current of the immunosensor first gradually increases and then begins to decrease. When the concentration of H_2O_2 is 5 mmol L^{-1}, the current response reaches the maximum. Therefore, the optimal concentration of the added H_2O_2 is selected to be 5 mmol L^{-1}.

3.5 Performances of the sandwich-type immunosensor

To assess the analytical performance of the immunosensor, the i–t technique is employed to detect various concentrations of SARS-CoV-2 NP under optimal experimental conditions. In Fig. 9a, the concentration of SARS-CoV-2 NP increases from 10 fg mL^{-1} to 20 ng mL^{-1}, resulting in a corresponding increase in the response current of the i–t curve. It can be attributed to the heightened specificity of the binding between SARS-CoV-2
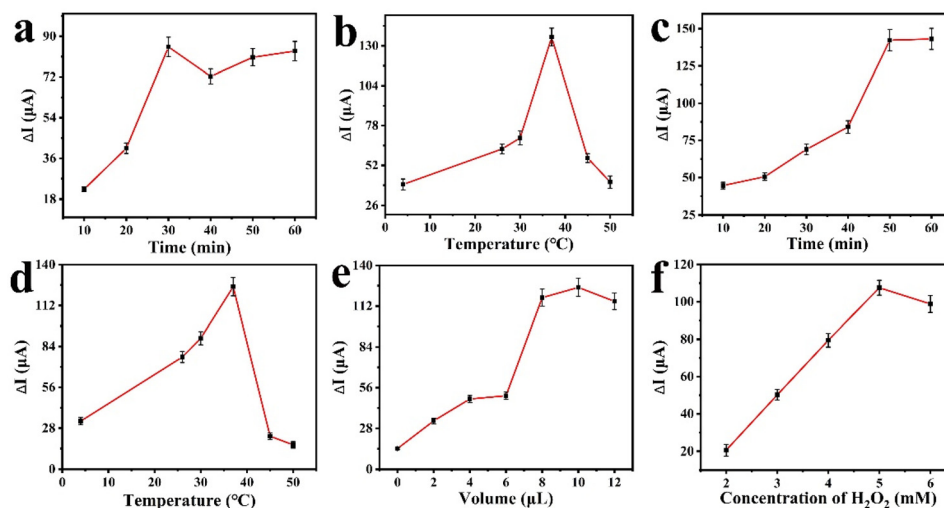

Fig. 8 Effect of the incubation time and incubation temperature of the antibody with SARS-CoV-2 NP (a and b) and signal probe of Ab_2-Au/Cu_2O (c and d); the volume of the signal probe (e); and the concentration of injected H_2O_2 (f) on the current change of the immunosensor incubated with 1.0 ng mL^{-1} SARS-CoV-2 NP in PBS solution after injecting 5 mmol L^{-1} H_2O_2.
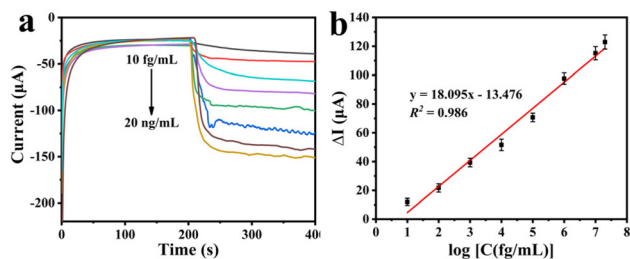
Fig. 9 (a) The *i−t* curves of different concentrations of SARS-CoV-2 NP detected with a sandwich-type immunosensor. (b) Linear calibration curve between the response current of the immunosensor and logarithm of the SARS-CoV-2 NP concentration.

NP and the signal probe Ab_2-Au/Cu_2O, while an augmentation in the presence of the Au/Cu_2O nanocomposite possesses excellent catalytic performance for H_2O_2. Consequently, the current signal generated by the reduction of H_2O_2 exhibits a continuous increase. Furthermore, there is an excellent linear correlation between the logarithm of the SARS-CoV-2 NP concentration and the response current. As shown in Fig. 9b, the linear calibration equation is $\Delta I = 18.095 \log[C \text{ (fg mL}^{-1})] - 13.476$ ($R^2 = 0.986$). The limit of detection (LOD) was calculated to be 1.12 fg mL^{-1} (S/N = 3). In Table S1,† compared to previously reported literature, the immunosensor shows superior performance in detecting SARS-CoV-2 NP.

3.6 Selectivity, reproducibility and stability

In order to study the specificity of the proposed analytical method, the selectivity of the immunosensor is investigated. The selected interfering substances are carcinoembryonic antigen (CEA), glucose (Glu), serine (Ser), neuron-specific enolase (NSE), prostate-specific antigen (PSA), uric acid (UA) and dopamine (DA). As shown in Fig. 10a, compared with SARS-CoV-2 NP (1.0 ng mL^{-1}), although the concentration of the above interfering substances is ten times that of SARS-CoV-2 NP, the immunosensor still shows a very low electrochemical response, indicating that the immunosensor has good specificity. In addition, the response current value of the mixed solution of interferents and SARS-CoV-2 NP is basically the same as those of the single SARS-CoV-2 NP, showing that the presence of interferents has little effect on the detec-
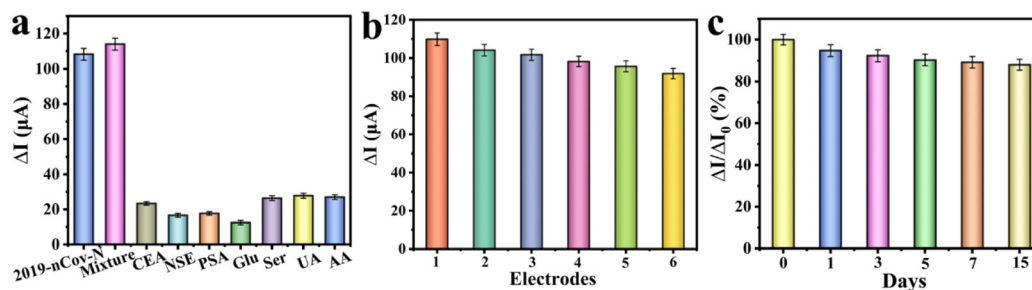
tion of SARS-CoV-2 NP. The result indicates that the immunosensor has excellent selectivity.

The repeatability and stability are also important indicators for evaluating the immunosensor. The concentration of SARS-CoV-2 NP is controlled to be 1.0 ng mL^{-1} to study the repeatability and stability of the immunosensor using the *i−t* technique. In Fig. 10b, six identical immune electrodes are prepared to detect SARS-CoV-2 NP, and the relative standard deviation (RSD, *n* = 6) between the detected response current values is 6.34%, indicating that the constructed immunosensing platform had good repeatability. As displayed in Fig. 10c, the assembled immunosensor is stored at 4 °C and tested at intervals. After 15 days of storage, the response current can still maintain 88.11% of the original current, which indicates that the immunosensor has desirable stability.

3.7 Analysis in human real serum samples

The analytical performance in human real serum samples was studied to evaluate the feasibility of the immunosensor in actual sample analysis. Under the optimal experimental conditions, SARS-CoV-2 NP with different concentrations was measured by the *i−t* technique with PBS solution (pH = 6.5) containing 10% pre-treated human actual serum samples as the electrolyte. In Fig. 11a, as the concentration of SARS-CoV-2 NP increases, the response current gradually increases. As shown in Fig. 11b, there is a linear correlation between the logarithm of the SARS-CoV-2 NP concentration and the peak current. The corresponding linear equation is $\Delta I = 12.777 \log$
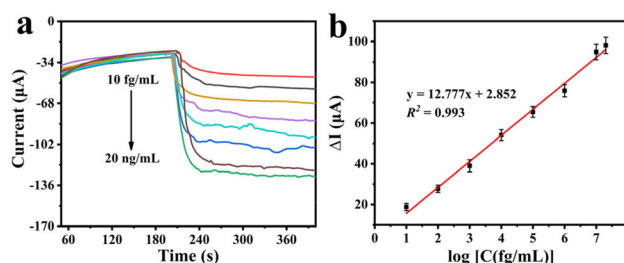

Fig. 11 (a) The *i−t* curves of different concentrations of SARS-CoV-2 NP in the actual serum. (b) Linear calibration curve between the response current of the immunosensor and logarithm of the SARS-CoV-2 NP concentration.

Fig. 10 (a) The selectivity test of the sandwich-type immunosensor towards SARS-CoV-2 NP (1.0 ng mL^{-1}), interferents (10 ng mL^{-1}), a mixture of interferents and SARS-CoV-2 NP. The reproducibility (b) and stability (c) tests of the sandwich-type immunosensor.

$[C \ (\text{fg mL}^{-1})] + 2.852 \ (R^2 = 0.984)$. The result indicates that the immunosensor possesses good practical application in the clinical detection of SARS-CoV-2 NP.

A certain concentration of SARS-CoV-2 NP is added to the actual human serum samples, and the corresponding recovery rate is measured using the standard addition method. As shown in Table S2,† the obtained recovery rates are between 92.00% and 106.85%, and the relative standard deviation (RSD, n = 3) is less than 7.60%, indicating that the immunosensor can be used to detect SARS-CoV-2 NP in human real serum samples.

4. Conclusions

In summary, a PANI/NiFeP nanosheet array-based electrochemical immunosensor using Au/Cu$_2$O nanocubes as a signal amplifier for the detection of SARS-CoV-2 NP is proposed. The PANI/NiFeP nanosheet arrays possess abundant amino groups, which can be used as the substrate material to ensure the effective immobilization of biomolecules. The introduction of the conductive substrate of nickel foam avoids the shortcomings of previous traditional adhesives. Au/Cu$_2$O nanocomposites as signal probes can efficiently catalyze the reduction of H$_2$O$_2$ to generate and amplify the current signal. Under the optimal experimental conditions, the assembled immunosensor exhibits outstanding analytical performance. It can also be used to detect SARS-CoV-2 NP in human serum samples with satisfactory recovery. The constructed immunosensor provides a new strategy for the detection of COVID-19 and has potential practical application value and broad application prospects in clinical diagnosis.

Author contributions

Liwei Bai: conceptualization, data curation, formal analysis, and writing – original draft. Yufen Shi: validation and formal analysis. Xue Zhang: formal analysis, validation, and methodology. Xiaowei Cao: formal analysis and methodology. Jianhua Jia: validation. Huanhuan Shi: formal analysis and review & editing. Wenbo Lu: methodology, project administration, review & editing, funding acquisition, and supervision.

Conflicts of interest

There are no conflicts to declare.

Acknowledgements

References

1 F. Wu, S. Zhao, B. Yu, Y. M. Chen, W. Wang, Z. G. Song, Y. Hu, Z. W. Tao, J. H. Tian, Y. Y. Pei, M. L. Yuan, Y. L. Zhang, F. H. Dai, Y. Liu, Q. M. Wang, J. J. Zheng, L. Xu, E. C. Holmes and Y. Z. Zhang, *Nature*, 2020, **579**, 265–269.

2 P. Zhang, L. Chen, J. Hu, A. Y. Trick, F. E. Chen, K. Hsieh, Y. Zhao, B. Coleman, K. Kruczynski, T. R. Pisanic II, C. D. Heaney, W. A. Clarke and T. H. Wang, *Biosens. Bioelectron.*, 2022, **195**, 113656.

3 A. Raziq, A. Kidakova, R. Boroznjak, J. Reut, A. Opik and V. Syritski, *Biosens. Bioelectron.*, 2021, **178**, 113029.

4 D. S. Chauhan, R. Prasad, R. Srivastava, M. Jaggi, S. C. Chauhan and M. M. Yallapu, *Bioconjugate Chem.*, 2020, **31**, 2021–2045.

5 C. Huang, Y. Wang, X. Li, L. Ren, J. Zhao, Y. Hu, L. Zhang, G. Fan, J. Xu, X. Gu, Z. Cheng, T. Yu, J. Xia, Y. Wei, W. Wu, X. Xie, W. Yin, H. Li, M. Liu, Y. Xiao, H. Gao, L. Guo, J. Xie, G. Wang, R. Jiang, Z. Gao, Q. Jin, J. Wang and B. Cao, *Lancet*, 2020, **395**, 497–506.

6 Q. Bayin, L. Huang, C. Ren, Y. Fu, X. Ma and J. Guo, *Talanta*, 2021, **227**, 122207.

7 S. Eissa and M. Zourob, *Anal. Chem.*, 2021, **93**, 1826–1833.

8 R. M. Torrente-Rodriguez, H. Lukas, J. Tu, J. Min, Y. Yang, C. Xu, H. B. Rossiter and W. Gao, *Matter*, 2020, **3**, 1981–1998.

9 X. Liu, L. Bai, X. Cao, F. Wu, T. Yin and W. Lu, *Anal. Chim. Acta*, 2022, **1234**, 340522.

10 I. C. Samper, C. J. McMahon, M. S. Schenkel, K. M. Clark, W. Khamcharoen, L. B. R. Anderson, J. S. Terry, E. N. Gallichotte, G. D. Ebel, B. J. Geiss, D. S. Dandy and C. S. Henry, *Anal. Chem.*, 2022, **94**, 4712–4719.

11 N. Kumar, N. P. Shetti, S. Jagannath and T. M. Aminabhavi, *Chem. Eng. J.*, 2022, **430**, 132966.

12 R. Zeng, M. Qiu, Q. Wan, Z. Huang, X. Liu, D. Tang and D. Knopp, *Anal. Chem.*, 2022, **94**, 15155–15161.

13 S. Lv, K. Zhang, L. Zhu, D. Tang, R. Niessner and D. Knopp, *Anal. Chem.*, 2019, **91**, 12055–12062.

14 R. Sakthivel, S. B. Prasanna, C. L. Tseng, L. Y. Lin, Y. F. Duann, J. H. He and R. J. Chung, *Small*, 2022, **18**, 2202516.

15 W. Bialobrzeska, M. Ficek, B. Dec, S. Osella, B. Trzaskowski, A. Jaramillo-Botero, M. Pierpaoli, M. Rycewicz, Y. Dashkevich, T. Lega, N. Malinowska, Z. Cebula, D. Bigus, D. Firganek, E. Biega, K. Dziabowska, M. Brodowski, M. Kowalski, M. Panasiuk, B. Gromadzka, S. Zoledowska, D. Nidzworski, K. Pyrc, W. A. Goddard III

and R. Bogdanowicz, *Biosens. Bioelectron.*, 2022, **209**, 114222.

16 S. Yadav, M. A. Sadique, P. Ranjan, R. Khan, N. Sathish and A. K. Srivastava, *J. Mater. Chem. B*, 2022, **10**, 8478–8489.

17 X. Pei, B. Zhang, J. Tang, B. Liu, W. Lai and D. Tang, *Anal. Chim. Acta*, 2013, **758**, 1–18.

18 J. Shu and D. Tang, *Anal. Chem.*, 2020, **92**, 363–377.

19 Z. Wang, X. Cao, D. Liu, S. Hao, G. Du, A. M. Asiri and X. Sun, *Chem. Commun.*, 2016, **52**, 14438–14441.

20 J. Li, M. Song, Y. Hu, C. Zhang, W. Liu, X. Huang, J. Zhang, Y. Zhu, J. Zhang and D. Wang, *Nano Res.*, 2023, **16**, 3658–3664.

21 X. Lei, S. Ge, Y. Tan, Z. Wang, J. Li, X. Li, G. Hu, X. Zhu, M. Huang, Y. Zhu and B. Xiang, *ACS Appl. Mater. Interfaces*, 2020, **12**, 9158–9168.

22 T. Chen, D. Liu, W. Lu, K. Wang, G. Du, A. M. Asiri and X. Sun, *Anal. Chem.*, 2016, **88**, 7885–7889.

23 S. Lv, K. Zhang, L. Zhu and D. Tang, *Anal. Chem.*, 2020, **92**, 1470–1476.

24 S. Lv, Y. Tang, K. Zhang and D. Tang, *Anal. Chem.*, 2018, **90**, 14121–14125.

25 X. Xu, T. Wang, C. Zhao, Z. Huang, M. Zheng, R. Jia and Y. Liu, *Microporous Mesoporous Mater.*, 2021, **312**, 110760.

26 B. Sun, Y. Wang, D. Li, W. Li, X. Gou, Y. Gou and F. Hu, *Mater. Sci. Eng., C*, 2020, **111**, 110797.

27 M. U. A. Prathap, C. I. Rodriguez, O. Sadak, J. Guan, V. Setaluri and S. Gunasekaran, *Chem. Commun.*, 2018, **54**, 710–714.

28 Y. Li, J. Xu, R. Cheng, J. Yang, C. Li, Y. Liu, R. Xu, Q. Wei and Y. Zhang, *Analyst*, 2022, **147**, 5178.

29 Y. Zhang, Z. Liu, Y. Wang, X. Kuang, H. Ma and Q. Wei, *J. Hazard. Mater.*, 2020, **398**, 122778.

30 B. Li, Y. Li, C. Li, J. Yang, D. Liu, H. Wang, R. Xu, Y. Zhang and Q. Wei, *Biosens. Bioelectron.*, 2023, **227**, 115180.

31 H. Ma, Y. Li, Y. Wang, L. Hu, Y. Zhang, D. Fan, T. Yan and Q. Wei, *Biosens. Bioelectron.*, 2016, **78**, 167–173.

32 H. Yang, H. Chen, L. Cao, H. Wang, W. Deng, Y. Tan and Q. Xie, *Talanta*, 2020, **212**, 120797.

33 F. X. Ma, F. Lyu, Y. Diao, B. Zhou, J. Wu, F. Kang, Z. Li, X. Xiao, P. Wang, J. Lu and Y. Y. Li, *Nano Res.*, 2021, **15**, 2887–2894.

34 J. Nai, S. Wang, Y. Bai and L. Guo, *Small*, 2013, **9**, 3147–3152.

35 A. Zhang, J. Wu, L. Xue, C. Li, S. Zeng, D. Caracciolo, S. Wang and C. J. Zhong, *ACS Appl. Mater. Interfaces*, 2021, **13**, 46577–46587.

36 L. Guan, L. Weng, N. Chen, H. Kannan, Q. Li, X. Zhang, Z. Wu, Y. Ma and A. Sahu, *Composites, Part A*, 2021, **147**, 106432.

37 B. Han, X. Ou, Z. Deng, Y. Song, C. Tian, H. Deng, Y. J. Xu and Z. Lin, *Angew. Chem., Int. Ed.*, 2018, **57**, 16811–16815.

38 F. Sun, G. Wang, Y. Ding, C. Wang, B. Yuan and Y. Lin, *Adv. Energy Mater.*, 2018, **8**, 1800584.

39 G. Hai, X. Jia, K. Zhang, X. Liu, Z. Wu and G. Wang, *Nano Energy*, 2018, **44**, 345–352.

40 J. Yu, G. Cheng and W. Luo, *J. Mater. Chem. A*, 2017, **5**, 11229–11235.

41 C. Zhang, N. Gong, C. Ding, Y. Li, W. Peng, G. Zhang, F. Zhang and X. Fan, *Int. J. Hydrogen Energy*, 2019, **44**, 26118–26127.

42 H. Liang, A. N. Gandi, C. Xia, M. N. Hedhili, D. H. Anjum, U. Schwingenschlögl and H. N. Alshareef, *ACS Energy Lett.*, 2017, **2**, 1035–1042.

43 H. Wang and S. Tao, *Nanoscale Adv.*, 2021, **3**, 2280–2286.

44 H. Chen, Y. Zou, J. Li, K. Zhang, Y. Xia, B. Hui and D. Yang, *Appl. Catal., B*, 2021, **293**, 120215.

45 S. Saha, N. Chaudhary, H. Mittal, G. Gupta and M. Khanuja, *Int. Nano Lett.*, 2019, **9**, 127–139.

46 H. Yan, L. Jiao, H. Wang, Y. Zhu, Y. Chen, L. Shuai, M. Gu, M. Qiu, W. Gu and C. Zhu, *Sens. Actuators, B*, 2021, **343**, 130108.

47 X. H. Li, J. J. Feng, W. J. Mao, F. Yin and J. Jiang, *J. Mater. Chem. C*, 2020, **8**, 14386–14392.